Soft Matter

RSC Publishing

PAPER

View Article Online
View Journal | View Issue

Cite this: *Soft Matter*, 2013, **9**, 7787

Suppression of the Rayleigh–Plateau instability on a vertical fibre coated with wormlike micelle solutions

F. Boulogne,*[a] M. A. Fardin,[bd] S. Lerouge,[cd] L. Pauchard[a] and F. Giorgiutti-Dauphiné[a]

Received 22nd December 2012
Accepted 17th June 2013

DOI: 10.1039/c3sm27940e

www.rsc.org/softmatter

We report on the Rayleigh–Plateau instability in films of giant micelle solutions coating a vertical fibre. We observe that the dynamics of thin films coating the fibre could be very different from the Newtonian or standard non-Newtonian cases. By varying the concentration of the components of the solutions and depending on the film thickness, we show for the first time that the Rayleigh–Plateau instability can be stabilized using surfactant solutions. Using global rheology and optical visualisations, we show that the development of shear-induced structures is required to stabilize the micellar film along the fibre. Assuming that the viscoelastic properties of the shear-induced state can be described by a simple model, we suggest that, in addition to the presence of shear-induced structures, the latter must have an elastic modulus greater than a critical value evaluated from a linear stability analysis. Finally, our analysis provides a way of estimating the bulk elasticity of the shear-induced state.

1 Introduction

When a liquid film is coating a fibre, it undergoes spatial thickness variations. The mechanism of this instability was understood by Lord Rayleigh in the 19th century.[1] Due to the energetic cost of free surfaces (surface tension), the liquid tends to minimize its surface area by breaking a cylinder into a series of regularly spaced droplets. This instability can be observed on free falling jets and it underlies many natural phenomena, like the dew drops on a cobweb.[2] The coating of fibres has been extensively studied by Quéré in the situation where the fibre is drawn out of a bath.[3] They compared their measurements with theoretical predictions from Landau, Levich and Derjaguin on the film thickness.[4,5]

In the case of a Newtonian fluid flowing down a vertical fibre, flow regimes have been depicted as a function of physical parameters. For high flow rates and/or fibre radii, the flow is dominated by inertia and the nature of the instability is convective.[6] In contrast, when the fibre size is smaller than the capillary length and for creeping flow (low Reynolds number), the instability is absolute and the physics is dominated by surface tension.[6] In such absolute regimes, we recently studied the flow of polymer solutions.[7] We investigated experimentally the influence of two non-Newtonian properties, shear-thinning effect and first normal stress difference, on the growth rate of the instability and on the morphology of the drops. The pattern is globally the same as in the case of Newtonian fluids: the first normal stress difference just tends to slightly decrease the growth rate and to smoothen the drop shape.

Besides polymers, a broad variety of molecules assemble to form non-Newtonian fluids. For instance, it is well-known that above a Critical Micellar Concentration (CMC), surfactant molecules can self-assemble to form aggregates called micelles. The size and the shape of the micelles depend on the structure of the surfactant molecule, on the surfactant concentration and on the presence of additives like simple or organic salts.[8] In some ranges of parameters, the micelles are giant worms often called "living polymers" because they can entangle like polymers but can also break and fuse continuously. Solutions of worm-like micelles present remarkable rheological properties such as shear-thickening or shear-banding effects, extensively studied by theoreticians and experimentalists.[9,10] These non-linear properties are often associated with the development of out of equilibrium structures induced by the shear flow. These shear-induced structures present strong viscoelastic properties leading to specific behaviors like the oscillation of a falling sphere[11] or the incomplete retraction of a filament after a pinch-off.[12] These examples highlight the consequence of the viscoelastic properties of the flow-induced phases.

In this paper, we investigate the flow, at low Reynolds number, along a vertical fibre of semi-dilute giant micelle solutions. By varying the concentration of the chemical compounds of the solutions and the thickness of the film along the fibre, we observe different morphologies for the micellar film. In some conditions, the film exhibits the expected Rayleigh–Plateau instability, as it has been observed so far, in

[a]*UPMC Univ Paris 06, Univ Paris-Sud, CNRS, Lab FAST, Bat 502, Campus Univ, Orsay, F-91405, France. E-mail: boulogne@fast.u-psud.fr; Fax: +33 1 69 15 80 60; Tel: +33 1 69 15 80 46*

[b]*Université de Lyon, Laboratoire de Physique, CNRS UMR 5672, École Normale Supérieure de Lyon, 46 Allée d'Italie, 69364 Lyon cedex 07, France*

[c]*Laboratoire Matière et Systèmes Complexes, CNRS UMR 7057, Université Paris Diderot, 10 rue Alice Domon et Léonie Duquet, 75205 Paris Cédex 13, France*

[d]*The Academy of Bradylogists.*

Newtonian fluids or viscoelastic polymer solutions while for other conditions, remarkably, the micellar film remains stable. Using global rheology and optical visualisations, we demonstrate that the stabilisation process along the fibre is connected with the development, above a characteristic shear stress, of shear-induced structures. We also show that the development of shear-induced structures is necessary but not sufficient to stabilize the micellar film. Using a simple viscoelastic model (Kelvin–Voigt) to describe the viscoelastic properties of the shear-induced state, we suggest that the elastic modulus characterizing the shear-induced structures has to be greater than a critical value provided by the linear stability analysis.

The paper is organized as follows. In Section 2, we present the experimental setup and the chemical system. In Section 3, we report different flow regimes depending on surfactant and/or salt concentrations and film thicknesses. In Section 4, we present the rheological behavior of our micellar systems and visualize the material under shear to confirm the presence of shear-induced structures. The next two sections are devoted to the conditions required to stabilize the micellar film on the fibre. Section 5 focuses on the stress applied to the film by gravity and its relationship with the rheological behaviour of the solution and Section 6 studies the role of the shear-induced film elasticity in the Rayleigh–Plateau instability.

2 Experimental details

2.1 Experimental setup

The experimental setup used for the study of the Rayleigh–Plateau instability is depicted in Fig. 1(a). An upper tank, of diameter 14 cm, is connected to a valve. This valve is composed of two axisymmetric cones. The adjustment of the gap between these cones controls the flow rate, *i.e.* the film thickness on the fibre. Guided by a nozzle, the liquid flows along a vertical nylon fibre. The fibre is about 60 cm long and has a radius $R = 0.28$ mm. Vertical position and centering of the nozzle are crucial to ensure an axisymmetric coating. This position is adjusted using an optical support with a precision of 2.4 arc s (Model U200-A2K, Newport). Observations are done with a telecentric lens and a high speed camera (about 500 images per s) delivering a resolution of 0.024 mm per pixel (Fig. 1(b) and (c)).

The rheological properties of the samples have been characterized using a stress-controlled rheometer (Anton Paar, MCR 501) at 20.00 ± 0.01 °C. The temperature was adjusted with a Peltier plate. We used a cone and plate geometry (radius 49.988 mm, angle 0.484°). A solvent trap was used to limit evaporation during the measurements. The rheological protocol consists in applying a stress sweep, the stress value being imposed for 1000 s at each step. The flow curve is obtained by averaging the shear rate response over the last 100 s of each step.

The global rheological measurements have been complemented by rheo-optical observations of the flow performed in a Taylor–Couette (TC) flow geometry (gap: 1.13 mm, length: 4 cm), adapted to the shaft of a stress-controlled rheometer (Anton Paar MCR 301). The inner cylinder rotates while the outer transparent cylinder is fixed in the laboratory frame. Direct visualizations were made in the plane velocity gradient/vorticity (*i.e.* the plane made by the radial direction and the cylinder's axis), the gap of the TC cell being illuminated with white light. Images of the gap were collected using a CCD camera. The rheological signal was recorded simultaneously, allowing direct correlation with optical visualizations.[13,14] Note that similar rheograms were obtained with TC and cone and plate geometries.

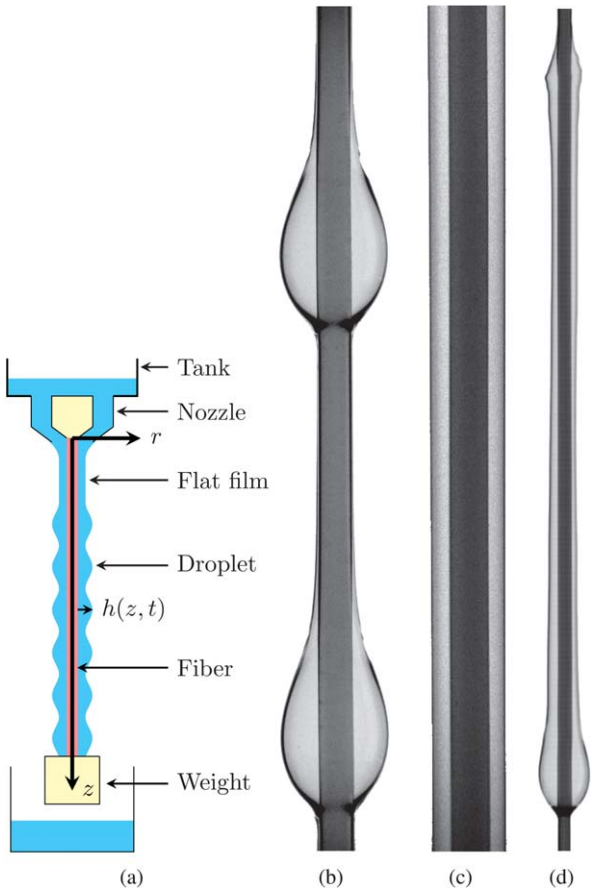

Fig. 1 (a) Notations and schematic view of the vertical fibre and the injection device. (b–d) Pictures illustrating the different morphologies of the film flowing along the fibre: (b) unstable morphology which corresponds to drops sliding on a quasi static liquid film. (c) Stable film. (d) Film morphology corresponding to a gel-like block moving down the fibre. The diameter of the fibre is 0.56 mm.

2.2 Materials

We focus on aqueous micellar solutions made of cetyltrimethylammonium bromide (CTAB) and sodium salicylate (NaSal) purchased from Sigma-Aldrich and used without further purification. Sodium salicylate is an organic salt, sometimes designated as a co-surfactant since it participates to the micellar structure by taking place in-between the polar head groups of surfactant molecules.[15] The addition of this salt also screens repulsive electrostatic interactions between CTA^+ groups and reduces the spontaneous curvature of the system.[16] As a result, the micellar uniaxial growth is promoted because of the large energetic cost of hemispherical endcaps. All the solutions investigated lie in the semi-dilute regime. For the range of

concentration chosen here, the micelles are locally cylindrical and slightly entangled.[9]

To prepare chemical solutions, we mixed in pure water (milliQ quality, resistivity: 18 MΩ cm) the weight percentages of NaSal and CTAB until complete dissolution occurred. Samples were stored at rest at 23 °C in darkness to avoid any degradation. The solutions were allowed to reach equilibrium for at least three days in these conditions before experiments were performed. We carefully checked the homogeneity of solutions before any measurement. All measurements along the fibre were carried out at $T = 20.0 \pm 0.5$ °C.

The equilibrium surface tension of the solutions studied in this paper is 36.0 ± 0.5 mN m^{-1} (Wilhelmy plate method with a Krüss tensiometer), a value consistent with measurements reported in the literature for solutions above the critical micellar concentration.[17]

3 Morphologies of the liquid film along a vertical fibre

We focused on low Reynolds number flows ($\mathrm{Re} \lesssim 1$) dominated by surface tension ($R < l_c = \sqrt{\frac{\gamma}{\rho g}} = 1.9$ mm), for which the flow is absolutely unstable.[6] We studied the flow along the vertical fibre of a large set of wormlike micelle solutions. Depending on the surfactant concentration [CTAB], the salt concentration [NaSal] and the film thickness h, we observe three possible morphologies of the film along the fibre as displayed in Fig. 1(b–d):

• The film can be unstable with respect to the Rayleigh–Plateau instability. The associated morphology corresponds to drops sliding on a quasi-static liquid film (Fig. 1(b)).

• The film can be stable and in this case, the associated morphology corresponds to a flat film (Fig. 1(c)).

• The film can be subjected to some kind of fracture leading to separate blocks moving down the fiber (Fig. 1(d)). The morphology is essentially flat but the film is discontinuous.

In order to illustrate the effect of the various parameters on the flow along the fibre, we construct a flow-phase diagram (see Fig. 2(a)) in the plane ([CTAB], [NaSal]), allowing identification of different domains.

At low NaSal concentrations, the apparent viscosity is low ($\lesssim$ 50 mPa s) which corresponds to inertial regimes.[6] At high NaSal concentrations, due to a high zero shear viscosity (>100 Pa s), the fluid hardly or could not flow through our experimental device ("no flow" domain). These two domains are excluded from the present study, which focuses on the intermediate range of NaSal concentrations, typically between 0.2 and 0.5 wt%. In this intermediate range, three domains, denoted by $\mathscr{A}$, $\mathscr{B}$ and $\mathscr{C}$, can be distinguished according to the sequence of morphologies observed as a function of the film thickness.

• Domain $\mathscr{A}$

In this domain, the micellar solutions behave as usual Newtonian fluids[6] or polymer solutions[7] for all the film thicknesses accessible with our experiment: the film is first flat and then the Rayleigh–Plateau instability develops (Fig. 1(b)).

• Domain $\mathscr{B}$

In this domain, regardless of the film thickness, the micellar solutions do not exhibit the Rayleigh–Plateau instability. For sufficiently small thicknesses (*i.e.* low flow rates), the film remains flat and continuous over the whole fibre extent (about 60 cm). From this stable morphology, an increase of the film thickness leads to breaking of the liquid thread into blocks of a few centimeters length, sliding along the fibre (Fig. 1(d)). Note that visually the blocks seem to have a gel-like character with a large elasticity, in contrast to the solutions at rest. Similar viscoelastic threads were observed in the case of pinch-off and filament retraction in extensional flow of wormlike micelles.[12,18]

• Domain $\mathscr{C}$

In between the two domains $\mathscr{A}$ and $\mathscr{B}$, domain $\mathscr{C}$ is characterized by the existence of the three morphologies (see Fig. 1(b–d)). For small thicknesses, the films are destabilized by the Rayleigh–Plateau instability with patterns similar to those described in domain $\mathscr{A}$. As its thickness is increased, the film adopts a stable morphology corresponding to a flat continuous liquid thread. Finally, for sufficiently large thicknesses, the flat and continuous liquid thread breaks into gel-like blocks as described in domain $\mathscr{B}$.

The different sequences of morphologies described above and observed respectively in the domains $\mathscr{A}$, $\mathscr{B}$ and $\mathscr{C}$ are schematized in Fig. 2(b).

When a stable morphology is observed, we have noticed that if we tilt the fibre horizontally, after a few seconds, drops can appear (Fig. 3). This observation suggests that the flow under the action of gravity is necessary to stabilize the film. Particularly, this shows that the flow properties of the micellar solutions are involved.

Note that this effect is different from the stabilizing process depicted by Quéré[19] with Newtonian fluids. In his experiments, stable films flowing down a vertical fibre were obtained by saturating the Rayleigh–Plateau instability thanks to the advection of the flows. This saturation (*i.e.* flat film) occurs if the film thickness is smaller than $h_c = \frac{R^3}{l_c^2}$. In our experiment, $h_c = 6$ μm while $h > 200$ μm, and the flow is absolutely unstable.

4 Rheo-optical properties under simple shear flow

In contrast to the free jets dominated by extensional flow,[20–22] the flow along the fibre is dominated by shear. We thus performed rheological experiments under simple shear flow in order to characterize the rheological properties of the micellar solutions used in this study. The measurement of the flow properties is combined with direct optical visualisations of the samples illuminated with white light in order to detect possible changes in the structure of the micellar fluid. In the different domains $\mathscr{A}$, $\mathscr{B}$ and $\mathscr{C}$ identified in the flow-phase diagram, we observe the same type of flow behaviour. Fig. 4(a) displays a

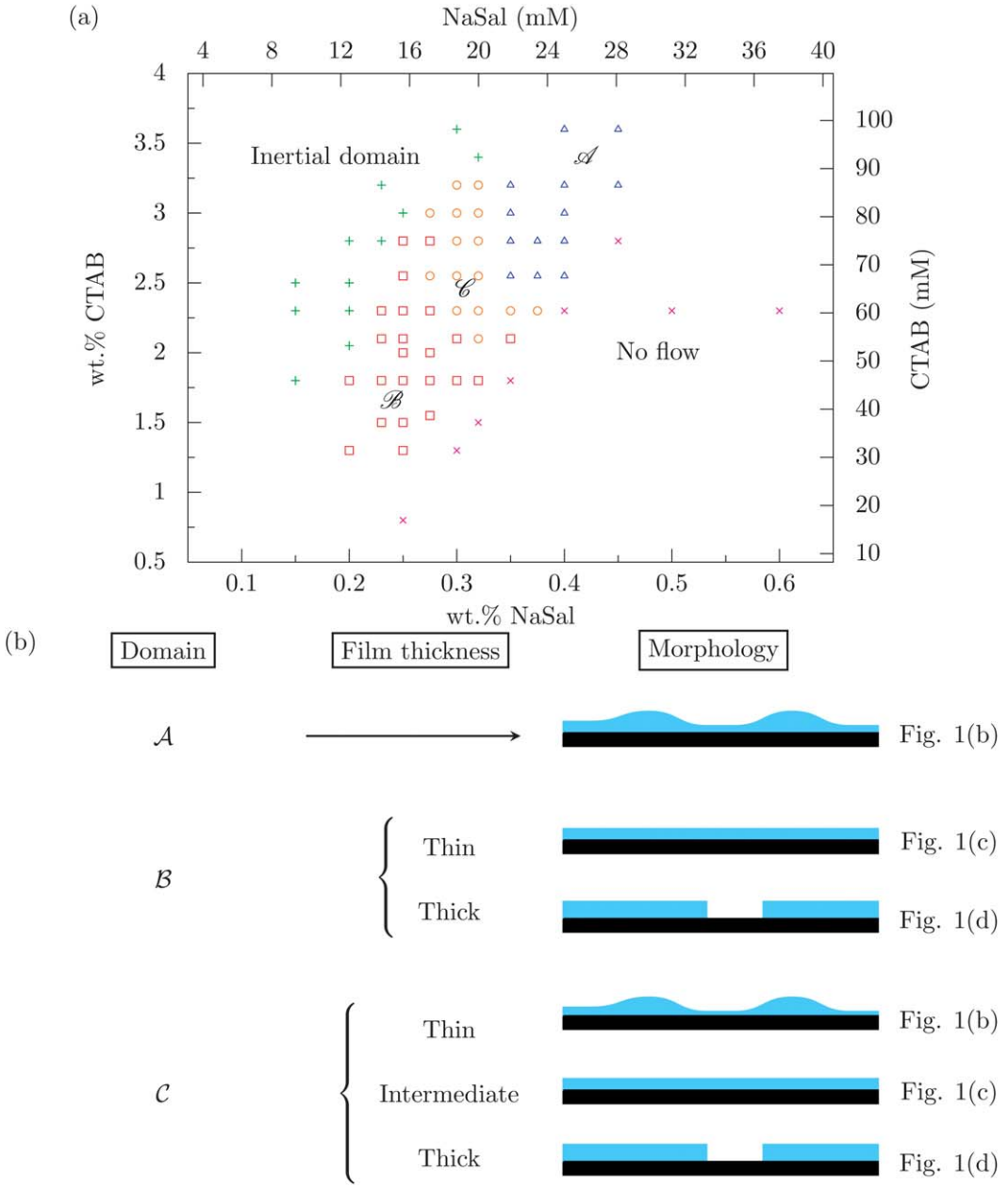

Fig. 2 (a) Flow-phase diagram showing domains depending on surfactant (CTAB) and cosurfactant (NaSal) concentrations. Five domains are identified: inertial (green +), "no flow" (magenta ×), $\mathscr{A}$ (blue △), $\mathscr{B}$ (red □) and $\mathscr{C}$ (orange ○). (b) Schematic representations of the different sequences of film morphologies as a function of the film thickness associated with the different domains $\mathscr{A}$, $\mathscr{B}$ and $\mathscr{C}$ in the flow-phase diagram.

representative flow curve gathered from a sample belonging to domain $\mathscr{C}$ and obtained in stress-controlled mode. The choice of this mode has been motivated by the fact that the maximum stress in the liquid flowing down the fibre can be easily estimated (see Section 5). The response of the samples to simple shear flow is highly nonlinear, with successive transitions, from shear-thickening to different degrees of shear-thinning. Such complex evolution of the shear stress as a function of the shear rate has already been observed for dilute micellar solutions, well-known to exhibit a shear-thickening transition.[23,24] Following ref. 23 and 24, we divide the flow curve into four distinct regimes, defined by "critical" shear stresses, denoted as σ_c, σ_s and σ_f.

- **Regime I ($\sigma < \sigma_c$)**

This regime corresponds to the primary response of the micellar solution to exceedingly low shear stresses. For dilute systems, we expect a linear increase of the shear stress as a function of the shear rate, associated with a Newtonian behaviour while for semi-dilute systems, a slight decrease of the viscosity as a function of the shear rate is usually observed, due to partial alignment of the micelles by the flow.[23,25] Unfortunately, reaching this regime requires shear stresses that cannot be imposed by the rheometer, which leads to the lack of experimental data points in Fig. 4. Note that in these conditions, σ_c is only roughly defined.

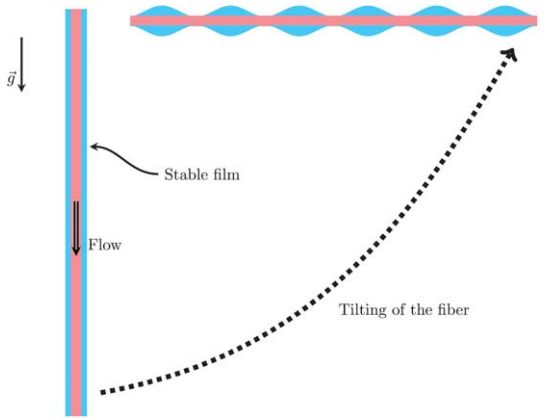

Fig. 3 From a vertical fibre where a stable film is flowing down, we tilt the fibre horizontally leading to the development of the Rayleigh–Plateau instability.

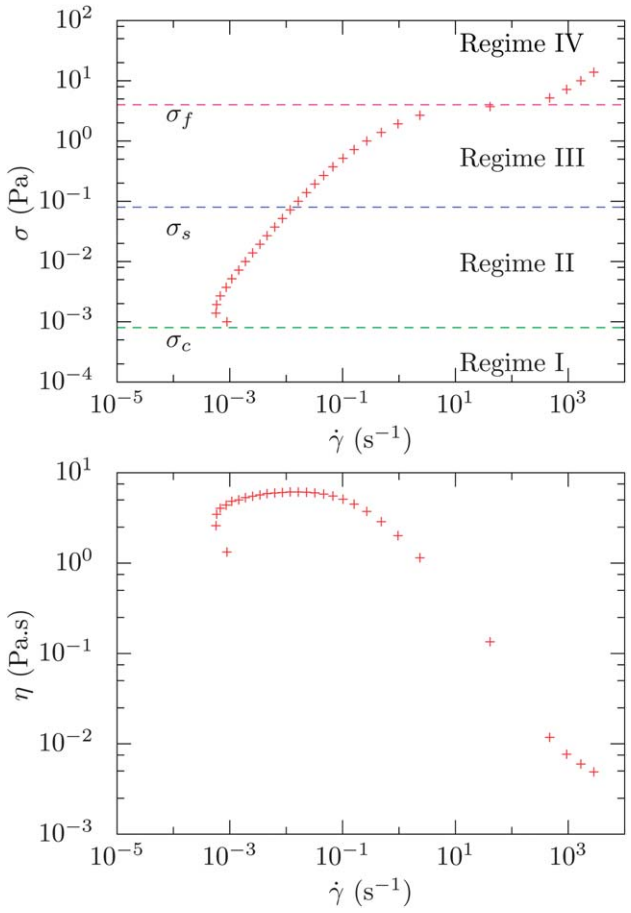

Fig. 4 (a) Shear stress σ and (b) apparent viscosity η as a function of the shear rate $\dot{\gamma}$ for a solution of CTAB (2.55 wt%) and NaSal (0.32 wt%). The temperature is $T = 20.00 \pm 0.01$ °C. The rheological protocol consists in a stress sweep experiment: at each step, the shear stress is kept fixed for 1000 s. The resulting shear rate $\dot{\gamma}(t)$ reaches a stationary value after a time period that depends on the applied shear stress. The flow curve is obtained by averaging the measured shear rate over the last 100 s of each step. σ_c, σ_s and σ_f denotes characteristic shear stresses that delimit different regimes in the flow curve.

• **Regime II ($\sigma_c < \sigma < \sigma_s$)**

This regime is characterized by a shear-thickening transition, the apparent viscosity of the material increasing with the shear rate (see Fig. 4). This transition is associated with a re-entrant behavior of the flow curve since the shear rate first decreases and then increases with the shear stress in this regime. Due to the re-entrant character of the transition, this regime can only be observed at imposed stress. The upper boundary of this regime is denoted as σ_s and corresponds to the shear stress for which the apparent viscosity reaches a maximum. Images of the sample in the shear-thickening regime do not exhibit any changes compared to the situation at rest. The gap of the TC cell appears homogeneous suggesting that the changes in the structure of the fluid associated with the shear-thickening transition occur at a sub-micronic scale.

• **Regime III ($\sigma_s < \sigma < \sigma_f$)**

In this range of applied stresses, the flow becomes shear-thinning and direct visualisations show that the gap of the TC cell remains homogeneous (see Fig. 6(a–c)).

• **Regime IV ($\sigma > \sigma_f$)**

This regime is characterized by a strong degree of shear-thinning associated with the existence of a stress plateau, the onset of which is denoted by a "critical" shear stress σ_f. The stress plateau generates a jump in the shear rate resulting in a sharp decrease of the apparent viscosity. The stress σ_f is determined by increasing the shear stress step by step with an appropriate sampling as illustrated in Fig. 5. The plateau is characterized by a large jump in the shear rate at imposed stress, or equivalently a strong increase of the shear rate *versus* time at fixed stress (see the inset in Fig. 5) and a large increase of the first normal stress difference N_1, indicative of nonlinear viscoelastic properties of the material under shear. Note that below or above σ_f, variations of the shear rate are lower than 10% over the duration of the measure (1000 s). For the sample in Fig. 5, we estimate $\sigma_f = 4.1 \pm 0.3$ Pa. In this regime, direct visualisations in the TC geometry reveal a drastic change in the structure of the fluid (see Fig. 6(d and e)). A fraction of the sample becomes slightly turbid leading to variations in the refraction index observable with visible light. These observations suggest that, for $\sigma > \sigma_f$, a new phase characterized by a length scale in the order of a few microns nucleates in the gap of the TC device.[26] We observed that the nucleation occurs from the edges of the cylinders and progressively extends along the inner cylinder, the growth being favoured at the bottom of the cell which has a conic shape. At fixed stress, the turbidity fluctuations observed on the pictures evolve in time with a complex dynamics. The proportion of the induced phase increases with the imposed shear stress, and for sufficiently high shear stresses, the induced phase invades the whole gap (see Fig. 6(f and g)). This scenario is reminiscent of the shear-banding transition even if there is no clear evidence for an organisation into two bands separated by a well-defined interface.[27] By monitoring the shear-rate as a function of time, we noticed that the appearance of the induced phase is

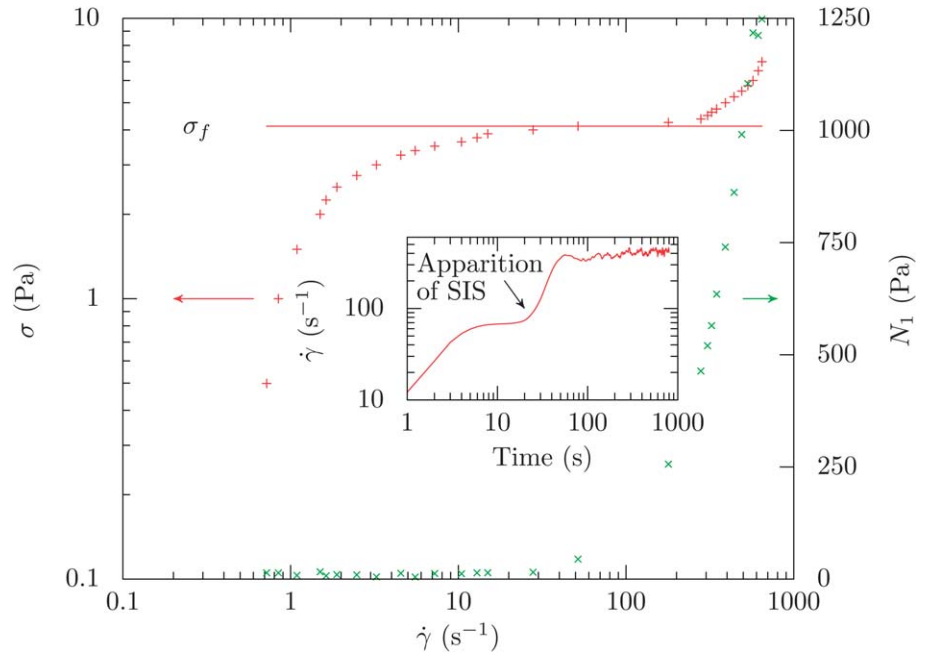

Fig. 5 Determination of the stress plateau value (σ_f). Stress σ (red +) and first normal stress difference N_1 (green ×) *versus* shear rate for 2.55 wt% CTAB and 0.32 wt% NaSal ($T = 20.00 \pm 0.01$ °C). At each step, the shear stress is imposed for 1000 s and the measured shear rate results from the average over the last 100 s of each step. Inset: time evolution of the shear rate $\dot{\gamma}$ for a fresh sample at $\sigma = 4.5$ Pa. The black arrow indicates the signature linked to the apparition of SIS.

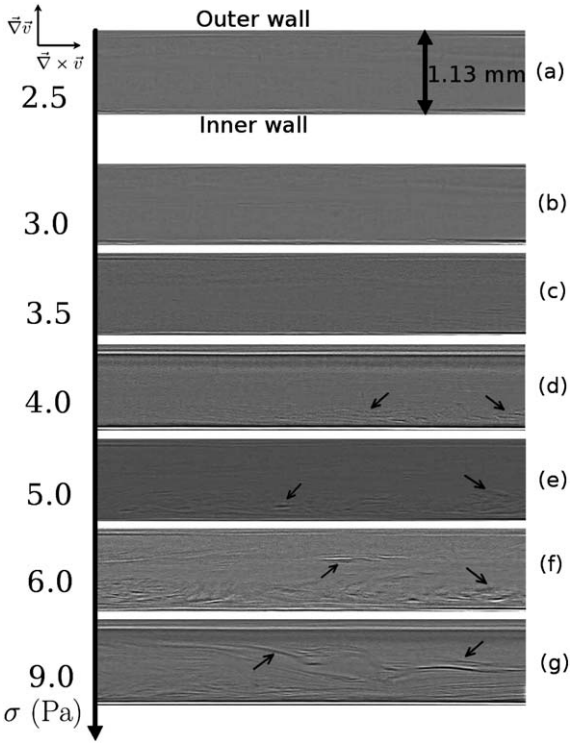

Fig. 6 Views of the gap of a Couette cell in the plane velocity gradient/vorticity (denoted as $(\vec{\Delta}\vec{v}, \vec{\Delta} \times \vec{v})$) for different applied shear stresses. Each image is taken after a time $t \sim 1000$ s. The solution is composed of 2.55 wt% CTAB and 0.32 wt% NaSal. The top and bottom sides correspond to the outer and inner wall respectively. For $\sigma > \sigma_f = 4$ Pa, structures appear near the inner wall. Arrows indicate some turbidity fluctuations indicative of SIS with a micronic characteristic length scale.

correlated with the presence of a kink in the $\dot{\gamma}(t)$ curve which appears sooner as the stress increases. This kink is also observed in the cone-plate geometry for $\sigma > \sigma_f$ (see the inset in Fig. 5) and is then the signature for the appearance of the induced phase.

Beyond this purely phenomenological description, our observations deserve further comments. As mentioned above, similar complex succession of rheological transitions in the flow curve has already been observed in dilute micellar solutions of TTAA/NaSal.[23,24] However, the direct observations reported by the authors largely differ from the present study: indeed, in the shear-thickening regime (regime II), the fluid phase of regime I was found to coexist with a viscous phase of gel-like shear-induced structures while in regime III, the induced gel-like phase invaded the whole gap of the flow geometry. Furthermore, the rheological response in regime III was also different, the apparent viscosity being constant, while in our case the system is shear-thinning. This behaviour was ascribed to the existence of a plug flow with slip at the walls. Finally, above σ_f, fracture of the gel-like phase followed by flow instabilities were observed.

Here we do not observe any phase coexistence in regime II. However, this does not rule out the fact that the shear-thickening transition is associated with a change of the structure of the system but rather suggests that this change of the structure occurs at a sub-micronic scale which prevents direct visualisation. Our situation could correspond to the minimal scenario for the shear-thickening transition in micellar systems, namely the uniaxial growth of the micelles.[27–30] On the other hand, we clearly observe a phase coexistence in regime IV, above σ_f, the induced phase being characterized by a large first-normal stress

difference. Note that, at equilibrium, the samples under investigation are only weakly entangled: their concentration is associated with the very beginning of the semi-dilute regime, in a "transition" range where the rheological behaviour is between pure shear-thickening of dilute rod-like micellar systems, and pure shear-banding of strongly entangled wormlike micelles.[27,31] In this context, the shear-banding-like behaviour observed in the present study is likely to correspond to a transition from the state induced during the shear-thickening regime (regime II) towards another induced "phase" structured at a larger scale (regime IV).

Note that in the literature on wormlike micelles, the shear-induced state associated with the shear-thickening transition was called SIS for shear-induced structure,[32] or SIP for shear-induced phase[33] interchangeably. Recent studies[34] have also used FISP to denote irreversible "flow-induced structured phase" obtained in extensional flow. However, in the present paper, we make no distinction between the expressions "shear-induced structures" and "shear-induced phase" and in the following we will refer to SIS as the reversible structures (or "phase") induced at a larger scale in regime IV.

5 Stress induced by gravity and development of shear-induced structures

As described in Section 3, the film morphology depends on the film thickness h. Our working hypothesis is that the transition between unstable and stable morphologies along the fibre might be linked to the presence of the SIS. To clarify and to go further on that point, we will focus on solutions in domain $\mathscr{C}$. This choice is motivated by the fact that solutions which belong to this domain present all three morphologies. We first study the influence of the CTAB concentration. We use a set of chemical solutions for which CTAB concentration is in the range of [1.8, 3.2]wt% keeping [NaSal] = 0.32 wt% constant. For each solution, we keep increasing the flow rate. The results are reported in Fig. 7 where we observe successively unstable, stable and block morphologies as the film thickness increases.

To explain this transition between stable and unstable morphologies, and since the rheology is controlled by the applied shear stress, we compare the stress plateau σ_f extracted from the rheological curves to the gravitational stress σ_g applied on the film. This stress $\sigma_g = \rho g h$ ranges between 2 and 8 Pa in our experiments and is then comparable to the value of the stress plateau σ_f. We define the film thickness h_f related to the stress plateau σ_f as $h_f = \sigma_f/(\rho g)$.

Fig. 7 illustrates the succession of film morphologies as a function of the film thickness h for different surfactant concentrations and a fixed salt concentration. We also report, for each sample, the value $h_f = \sigma_f/(\rho g)$ gathered from the rheological experiments. Remarkably, the unstable–stable transition is found to occur as $h \simeq h_f$. Thus, we can conclude that the condition $\sigma_g > \sigma_f$ is necessary to stabilize the film. This suggests that the stabilization of the film is connected to the presence of the SIS as σ_f is the characteristic stress value for the development of these structures.

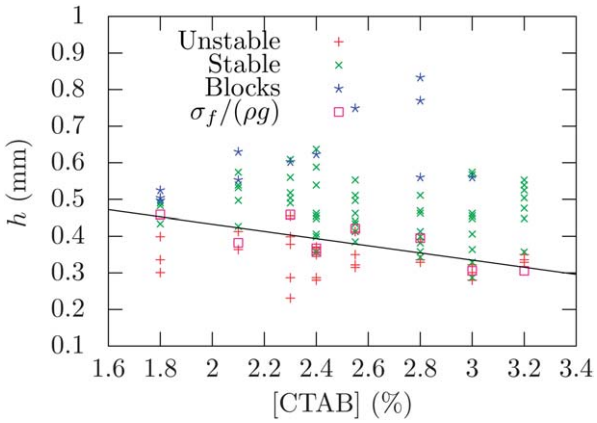

Fig. 7 Film morphologies for different film thicknesses and various surfactant concentrations ([NaSal] = 0.32 wt%). The black line is a fit of film thicknesses $h_f = \sigma_f/(\rho g)$ (□) related to stress plateau values. It separates unstable and stable flow regimes.

Consequently, the SISs could be formed, before the Rayleigh–Plateau instability acts, if $\sigma > \sigma_f$. This fixes the first condition to stabilize the film. As we will see in the next section, this condition is necessary but not sufficient.

6 Effect of the SIS elasticity on the instability growth rate

In this section, we study a second set of chemical solutions in order to complete our understanding. The question we attempt to answer is: why do films suddenly become always unstable if the concentrations are slightly changed near the border between domains $\mathscr{A}$ and $\mathscr{C}$? To cross these two domains, we work with a constant CTAB concentration ([CTAB] = 2.55 wt%) while NaSal concentrations vary in the range [0.25, 0.4] wt%. Fig. 8 displays the film morphology as a function of thickness for different salt concentrations covering domains $\mathscr{A}$ and $\mathscr{C}$ at a fixed surfactant concentration. Based on rheological data, the thickness of the film $\sigma_f/(\rho g)$ beyond which the SISs are likely to

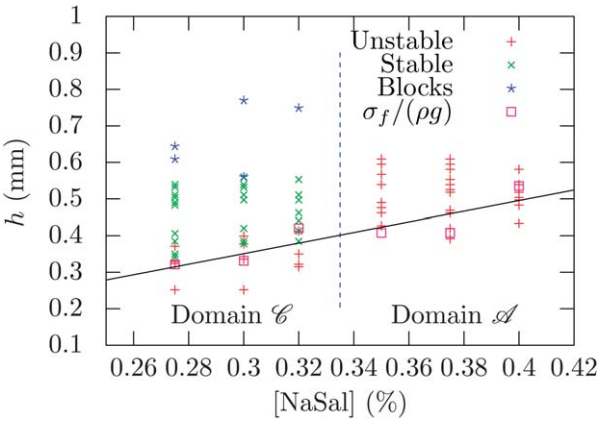

Fig. 8 Film morphologies for different film thicknesses and various salt concentrations ([CTAB] = 2.55 wt%). The black line is a fit of film thicknesses $h_f = \sigma_f/(\rho g)$ related to stress plateau values.

develop is also reported. A good agreement is again observed in domain $\mathscr{C}$ between the expected thickness computed from rheological results and the effective thickness above which the films are stable. However, there is a discrepancy for solutions in domain $\mathscr{A}$ since films thicker than h_f are unstable. According to our analysis, the SISs still develop but they do not stabilize the film.

To understand these observations, we focus on two effects: the surface tension which is responsible for the instability and the bulk elasticity which tends to slow down the film deformations.

It is worth noting that the constitutive relationship describing the SIS is still unknown. Since SISs present strong elastic properties, we attempt a description of the SIS by a simple Kelvin–Voigt model allowing analytical calculations.[35,36] The Kelvin–Voigt model takes into account the viscous dissipation at short time scales and elasticity at long time scales. The stress tensor σ_{ij} is a function of two parameters: viscosity η_0 and elastic modulus G_0:

$$\sigma_{ij}(t) = G_0\varepsilon_{ij} + \eta_0\dot{\varepsilon}_{ij} \quad (1)$$

where ε_{ij} is the strain and the dot represents the time derivative.

To obtain the dispersion relationship for this constitutive equation, we perform a linear stability calculation. The Fourier transform of expression (1) reduces the equation to

$$\sigma_{ij}(\omega) = \eta(\omega)\dot{\varepsilon}_{ij}(\omega) \quad (2)$$

where ω is a complex frequency and with $\eta(\omega) = \frac{iG_0}{\omega} + \eta_0$.

Experimentally, we observe that the film thicknesses $h(z)$ and the fibre radius R have the same order of magnitude. Under this consideration, we can calculate the dispersion relationship in our geometry.[37]

In the cylindrical reference frame (r, θ, z) (see Fig. 1(a)), the z-component of the momentum balance, taking into account the lubrication approximation, becomes:

$$\rho g - \partial_z p + \frac{\eta}{r}\partial_r(r\partial_r u) = 0 \quad (3)$$

where u is the fluid velocity along the fibre (z direction). The boundary conditions are: no-slip on the fibre ($u(r = R) = 0$) and zero tangential stress at the liquid–air interface ($\partial_r u(r = R + h) = 0$). The pressure gradient is caused by surface curvatures and it is expressed from Laplace's law: $\partial_z p = -\gamma\left(\frac{\partial_z h}{(R+h)^2} + \partial_{zzz}h\right)$ (assuming $\partial_z h \ll 1$). Solving this equation, the fluid velocity profile is $u(r) = \frac{\partial_z p - \rho g}{4\eta}\left[\left(r^2 - R^2\right) - 2\left(R + h\right)^2 \ln\left(\frac{r}{R}\right)\right]$.

Incompressibility leads to:

$$\frac{\partial h}{\partial t} + \frac{\partial q}{\partial z} = 0 \quad (4)$$

where the flow rate per unit length is $q = \frac{1}{2\pi(R+h)}\int_R^{R+h} u(r)\,2\pi r\mathrm{d}r$.

To conduct a linear stability analysis, we develop the film thickness as $h = h_0 + h_1 e^{i(kz-\omega t)}$ where k is the real wavenumber. Thus, we derive the following dispersion relationship

$$\omega = k\frac{\rho g R^2\psi(\alpha)}{16\eta(\omega)} - i\frac{\gamma R h_0^3\phi(\alpha)}{3\eta(\omega)(R+h_0)}\left(k^4 - \frac{k^2}{(R+h_0)^2}\right) \quad (5)$$

with $\alpha = h_0/R$. Two dimensionless functions reflect the geometry:

$$\psi(x) = \frac{-x(2+x)\left(6+5x(2+x)\right) + 12(1+x)^4\ln(1+x)}{(1+x)^2}$$

and

$$\phi(x) = \frac{3\left(4(x+1)^4\ln(x+1) - x(x+2)(3x(x+2)+2)\right)}{16x^3}$$

The imaginary part of ω corresponds to the instability growth rate denoted as $\Omega(k)$:

$$\Omega(k) = \frac{-\gamma R h_0^3\phi(\alpha)}{3\eta_0(R+h_0)}\left(k^4 - \frac{k^2}{(R+h_0)^2}\right) - \frac{G_0}{\eta_0} \quad (6)$$

For $\Omega(k) < 0$, the system is stable, whereas for $\Omega(k) > 0$ the system is unstable. If $G_0 = 0$, the solution for Newtonian fluids is recovered. The evolution of the growth rate with k is plotted in Fig. 9.

We observe that the bulk elasticity (G_0) plays a stabilizing effect on the film as illustrated in Fig. 9: the marginal stability curve is shifted to the negative Ω. If $\max(\Omega) = \Omega(k_{max}) < 0$ (blue curve in Fig. 9), all modes are damped by the elasticity resulting in a stable film.

Note that, in this model, the wavenumber for the maximum of the growth rate is $k_{max} = \frac{1}{\sqrt{2}(R+h_0)}$ and is independent of the elastic modulus.

Solving the condition $\Omega(k_{max}) = 0$ defines a critical elastic modulus G_0^c:

$$G_0^c(h) = \frac{\gamma h^3 R\phi(h/R)}{12(R+h)^5} \quad (7)$$

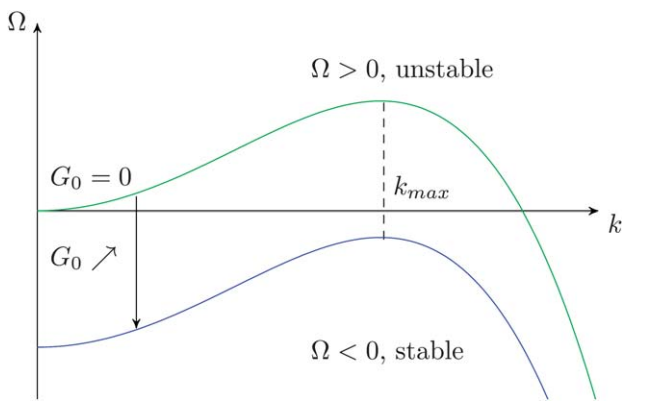

Fig. 9 Growth rate of the instability Ω *vs.* the wavenumber k from the Kelvin–Voigt model illustrating the stabilizing effect of the bulk elasticity G_0. The case $G_0 = 0$ (in green) is the marginal stability curve for Newtonian fluids (viscosity η_0). As G_0 increases, the marginal curve (in blue) is shifted to the negative growth rate domain.

Experimentally, we can estimate G_0^c from the border between domains $\mathscr{A}$ and $\mathscr{C}$. From the data presented in Fig. 8, we can evaluate for [CTAB] $\simeq$ 2.55 wt% $\simeq$ 70 mM, [NaSal] $\simeq$ 0.33 wt% $\simeq$ 20 mM: $G_0 \simeq G_0^c(h_f) = 1.0$ Pa (with $h = h_f = 0.4$ mm).

Thus the bulk elasticity of the SIS has to be sufficient to shift the curve of the growth rate to the negative values, in order to stabilize the film. To summarize, we have shown that the elastic shear induced structures are developed in our flow if $\rho g h > \sigma_f$. If this condition is fulfilled, we expect a stable film only if the bulk elasticity is greater than G_0^c. As a result, we can explain the apparent discrepancy of the unstable region in Fig. 8. From the transient zone to the unstable one (*i.e.* increasing salt concentration), the bulk elasticity decreases such that $G_0 < G_0^c$.

The value $G_0^c = 1$ Pa can be compared to oscillatory shear flow tests. As suggested by the flow curve in Fig. 4, the linear regime could not be reached with our rheometer. The first test consists in the measurement of the elastic modulus *versus* time for a shear stress amplitude of 5×10^{-4} Pa at a frequency $f = 1$ Hz. The elastic modulus increases with time from $\sim 10^{-2}$ Pa to a few Pascal ([CTAB] = 2.55 wt% and [NaSal] = 0.32 wt%). In a second test, a constant shear stress $\sigma > \sigma_f$ is applied to the sample followed by an oscillating stress of small amplitude. Even if the SIS has time to partially relax, such experiments can provide a reasonable order of magnitude of the moduli (G' and G'') of the SIS at high angular velocities. We found a value for the elastic modulus around 1.5 Pa, consistent with the value $G_0^c = 1$ Pa gathered from the flow along the fibre and considering that the viscoelastic properties of the SIS can be modelled by a Kelvin–Voigt model. Our results suggest that the elastic modulus of the solutions under shear is larger than the one for the solution at rest and that the value required to stabilize the flow could be deduced from the Kelvin–Voigt model.

7 Conclusion

In this paper, we studied the flow of CTAB/NaSal solutions on a vertical fibre. Structure modifications occurring from the chemical composition and the shear flow provide a large variety of flowing regimes. The flow on the fiber can actually be unstable and similar to the flow of Newtonian fluids: the capillary driven Rayleigh–Plateau instability produces drops sliding on the fibre. For another set of solutions, the film can stay uniform along the fiber provided the film thickness satisfies the condition $h > h_f = \sigma_f/(\rho g)$. From rheo-optical measurements, we found that the condition for stabilizing the flow is that the characteristic stress on the film should be larger than a critical stress σ_f. This critical stress has been identified as the onset of emergence of micronic structures induced by the shear-flow, *i.e.*, shear-induced structures (SISs). A last flowing regime is observed for high film thicknesses and in a given range of concentrations: in this last regime, the film breaks into a series of gel-like blocks sliding along the fibre.

Our analysis suggests that the bulk elasticity of the SIS is responsible for the decrease of the instability growth rate until inhibition by the Rayleigh–Plateau instability for a negative growth rate. Two conditions are required to prevent the destabilization of the film: the presence of the SIS and a sufficient elasticity of these structures to inhibit the instability driven by the surface tension. A linear analysis of stability assuming a Kelvin–Voigt model for SIS evidences a stable flow provided the elastic modulus of the SIS is higher than a critical value. By comparing with experimental results on systems which can go through an unstable to stable regime, we can estimate the value of the elastic modulus of these SISs. In the future, the inspection of the micronic SIS can provide a better understanding of the micellar structure inducing the bulk elasticity.

Acknowledgements

The authors thank Triangle de la Physique for the rheometer (Anton Paar, MCR 501) and Fédération Paris VI for the high-speed camera. Also, thanks to Jérôme Delacotte, Christophe Clanet and Marina Moreno Luna for discussions.

References

1 L. Rayleigh, *Proc. Lond. Math. Soc.*, 1878, **s1–10**, 4–13.
2 C. Boys, *Soap Bubbles: Their Colors and Forces Which Mold Them*, Thomas Y. Crowell Company, 1959.
3 D. Quéré, *Annu. Rev. Fluid Mech.*, 1999, **31**, 347–384.
4 L. Landau and B. Levich, *Acta Physicochim. URSS*, 1942, **17**, 42–54.
5 B. Derjaguin, *Acta Physicochim. URSS*, 1943, **20**, 349–352.
6 C. Duprat, C. Ruyer-Quil, S. Kalliadasis and F. Giorgiutti-Dauphiné, *Phys. Rev. Lett.*, 2007, **98**, 244502.
7 F. Boulogne, L. Pauchard and F. Giorgiutti-Dauphiné, *J. Fluid Mech.*, 2012, **704**, 232.
8 J. N. Israelachvili, *Intermolecular and Surface Forces*, Academic Press, 2011.
9 J. Berret, in *Rheology of wormlike micelles: equilibrium properties and shear banding transitions*, Springer, 2006, pp. 667–720.
10 M. E. Cates and S. M. Fielding, *Adv. Phys.*, 2006, **55**, 799–879.
11 A. Jayaraman and A. Belmonte, *Phys. Rev. E: Stat., Nonlinear, Soft Matter Phys.*, 2003, **67**, 065301.
12 L. B. Smolka and A. Belmonte, *J. Non-Newtonian Fluid Mech.*, 2003, **115**, 1–25.
13 S. Lerouge, M. Fardin, M. Argentina, G. Grégoire and O. Cardoso, *Soft Matter*, 2008, **4**, 1808–1819.
14 M. A. Fardin, B. Lasne, O. Cardoso, G. Grégoire, M. Argentina, J. P. Decruppe and S. Lerouge, *Phys. Rev. Lett.*, 2009, **103**, 028302.
15 U. Rao, C. Manohar, B. S. Valaulikar and R. M. Iyer, *J. Phys. Chem.*, 1987, **91**, 3286–3291.
16 Z. Lin, J. J. Cai, L. E. Scriven and H. T. Davis, *J. Phys. Chem.*, 1994, **98**, 5984–5993.
17 J. J. Cooper-White, R. C. Crooks and D. V. Boger, *Colloids Surf., A*, 2002, **210**, 105–123.
18 A. Bhardwaj, E. Miller and J. Rothstein, *J. Rheol.*, 2007, **51**, 693–719.
19 D. Quéré, *Europhys. Lett.*, 1990, **13**, 721.
20 C. Clasen, J. Eggers, M. Fontelos, J. Li and G. McKinley, *J. Fluid Mech.*, 2006, **556**, 283–308.

21 J. Eggers and E. Villermaux, *Rep. Prog. Phys.*, 2008, **71**, 036601.
22 P. Bhat, S. Appathurai, M. Harris, M. Pasquali, G. McKinley and O. Basaran, *Nat. Phys.*, 2010, **6**, 625–631.
23 Y. T. Hu, P. Boltenhagen and D. J. Pine, *J. Rheol.*, 1998, **42**, 1185–1208.
24 Y. T. Hu, P. Boltenhagen, E. Matthys and D. J. Pine, *J. Rheol.*, 1998, **42**, 1209–1226.
25 V. Hartmann and R. Cressely, *Europhys. Lett.*, 1997, **40**, 691–696.
26 B. A. Schubert, N. J. Wagner, E. W. Kaler and S. R. Raghavan, *Langmuir*, 2004, **20**, 3564–3573.
27 S. Lerouge and J.-F. Berret, *Adv. Polym. Sci.*, 2010, **230**, 1–71.
28 J.-F. Berret, R. Gamez-Corrales, Y. Séréro, F. Molino and P. Lindner, *Europhys. Lett.*, 2001, **54**, 605–611.
29 B. Prötzl and J. Springer, *J. Colloid Interface Sci.*, 1997, **190**, 327–333.
30 R. Oda, V. Weber, P. Lindner, D. Pine, E. Mendes and F. Schloesser, *Langmuir*, 2000, **14**, 4859–4863.
31 V. Hartmann and R. Cressely, *Colloids Surf., A*, 1997, **121**, 151–162.
32 D. Ohlendorf, W. Interthal and H. Hoffmann, *Rheol. Acta*, 1986, **25**, 468–486.
33 P. Boltenhagen, Y. Hu, E. Matthys and D. Pine, *Europhys. Lett.*, 1997, **38**, 389–394.
34 M. Vasudevan, E. Buse, D. Lu, H. Krishna, R. Kalyanaraman, A. Q. Shen, B. Khomami and R. Sureshkumar, *Nat. Mater.*, 2010, **9**, 436–441.
35 S. A. Safran and J. Klein, *J. Phys. II*, 1993, **3**, 749–757.
36 F. Closa, F. Ziebert and E. Raphaël, *Math. Modell. Nat. Phenom.*, 2012, **7**, 6–19.
37 C. Duprat, C. Ruyer-Quil and F. Giorgiutti-Dauphiné, *Phys. Fluids*, 2009, **21**, 042109.

